Monitoring Oxygen Production on Mass-Selected Iridium-Tantalum Oxide Electrocatalysts

Ya-Rong Zheng[1,2†], Jerome Vernieres[1†], Zhenbin Wang[1†], Ke Zhang[1†], Degenhart Hochfilzer[1], Kevin Krempl[1], Ting-Wei Liao[1], Francesco Presel[1,3], Thomas Altantzis[4,5], Jarmo Fatermans[4], Soren Bertelsen Scott[1], Niklas Mørch Secher[1], Choongman Moon[1], Pei Liu[4], Sara Bals[4], Sandra Van Aert[4], Ang Cao[1], Megha Anand[1], Jens K. Nørskov[1*], Jakob Kibsgaard[1], and Ib Chorkendorff[1*]

[1]*Department of Physics, Technical University of Denmark, 2800 Kongens Lyngby, Denmark.*

[2]*Anhui Province Key Laboratory of Advanced Catalytic Materials and Reaction Engineering, School of Chemistry and Chemical Engineering, Hefei University of Technology, 230009, Hefei, China.*

[3]*Institute of Physics, NAWI Graz, University of Graz, Universitätsplatz 5, 8010 Graz, Austria.*

[4]*EMAT and NANOlab Center of Excellence, University of Antwerp, Groenenborgerlaan 171, 2020 Antwerp, Belgium.*

[5]*ELCAT, University of Antwerp, Universiteitsplein 1, 2610 Wilrijk, Belgium.*

[†]These authors contributed equally: Y.-R. Zheng, J. Vernieres, Z. Wang, K. Zhang.

*Corresponding authors, e-mail: ibchork@fysik.dtu.dk and jkno@dtu.dk

Development of low-cost and high-performance oxygen evolution reaction catalysts is key to implementing polymer electrolyte membrane water electrolyzers for hydrogen production. Iridium-based oxides are the state-of-the-art acidic oxygen evolution reaction catalysts but still suffer from inadequate activity and stability, and iridium's scarcity motivates the discovery of catalysts with lower iridium loadings. Here we report a mass-selected iridium-tantalum oxide catalyst prepared by a magnetron-based cluster source with considerably reduced noble-metal loadings beyond a commercial IrO_2 catalyst. A sensitive electrochemistry/mass-spectrometry instrument coupled with isotope labelling was employed to investigate the oxygen production rate under dynamic operating conditions to account for the occurrence of side reactions and quantify the number of surface active sites. Iridium-tantalum oxide nanoparticles smaller than 2 nm exhibit a mass activity of 1.2 ± 0.5 kA g_{Ir}^{-1} and a turnover frequency of 2.3 ± 0.9 s^{-1} at 320 mV overpotential, which are two and four times higher than those of mass-selected IrO_2, respectively. Density functional theory calculations reveal that special iridium coordinations and the lowered aqueous decomposition free energy might be responsible for the enhanced performance.

Water electrolysis ($2H_2O \rightarrow 2H_2 + O_2$) driven by renewable power sources (for example, solar and wind) offers a sustainable strategy to store energy in the form of hydrogen fuel[1,2]. The polymer electrolyte membrane water electrolyzer (PEM-WE) operating in acidic media serves as a promising technology for such energy conversion and is preferable to alkaline conditions for hydrogen production because of its high current density, fast response, stable operation performance and low cross-over under pressurized

operating conditions[3]. However, the sluggish anodic oxygen evolution reaction (OER), along with the

challenge of materials' stability under the harsh working conditions (low pH, high potentials > 1.4 V, high

oxygen concentration on the anode), severely limits the choice of electrocatalyst and hinders the device

applications on a large scale[4].

As of now, anode catalysts are primarily built on scarce iridium (Ir)[5-7]. Either searching for earth-abundant alternatives or developing catalysts with a minimized Ir loading could be a feasible strategy.

Considering the global Ir resource and its catalytic performance towards the OER, a 40 times reduction of

the Ir loading (from currently ~ 2 mg_{Ir} cm^{-2} to less than 0.05 mg_{Ir} cm^{-2}) and an enhanced intrinsic activity

are highly needed to facilitate the widespread implementation of PEM-WE[8]. Many approaches have been

conducted to reduce the Ir consumption and improve the activity of Ir-based catalysts, such as dispersing

Ir into inexpensive supports[9,10], manipulating the surface area by nanostructuring[11] and engineering the

reconstructed IrO_x surfaces by leaching[12,13]. Nevertheless, to preserve a reasonable activity and

conductivity, loadings of > 20 wt% are still required[10,14,15]. In addition, further performance improvement

of Ir-based catalysts is limited by finding an acid-stable matrix that has a good electronic conductivity

even at high anodic potentials. Inspired by the electron tunnelling phenomenon in semiconductors,

corrosion-resistant metal oxides (Ta_2O_5, Sb_2O_5, and HfO_2) in the subnanoscale could be sufficiently

conductive for electrocatalysis, despite having a wide bandgap in bulk[16,17]. More important, it is critical

to unambiguously evaluate the intrinsic oxygen evolution activity. The OER is a rather complex process,

always accompanied by other side reactions, for example, oxidation of adventitious carbon,

catalyst/support oxidation, material dissolution and capacitive current effects, which could lead to an

1   overestimation of the actual OER activity of a catalyst[18,19]. Therefore, the OER should always be

2   quantified by measuring the actual oxygen production.

3   Here, we develop a catalyst of iridium-tantalum oxide (Ir-Ta-O) for OER by using a stable Ta_2O_5

4   nanocluster as the matrix. The mass-selected Ir-Ta-O catalysts with sizes ranging from cluster to particle

5   regime have been precisely synthesized by an ultrahigh-vacuum cluster source technique[20]. The actual

6   OER activity of mass-selected catalyst has been accurately evaluated based on a silicon (Si) microchip-

7   based electrochemistry/mass-spectrometry (EC-MS) instrument, developed by our prior work, which has

8   a time resolution of seconds and 100 % collection efficiency[21]. We find that the catalyst within a small

9   size regime (< 2 nm) exhibits a mass activity of 1.2 ± 0.5 kA_{O_2} g_{Ir}^{-1} and a turnover frequency (TOF) of 2.3

10   ± 0.9 s^{-1} at 320 mV overpotential, along with an enhanced stability in acidic media. Density functional

11   theory (DFT) calculations further uncover the key factors dictating these improved activity and stability.

12   **Preparation and characterization of mass-selected Ir-Ta-O.** Herein, we synthesized up to 12

13   distinctive masses from 6.0×10^3 to 6.0×10^5 atomic mass unit (amu) particles, using our well-established

14   ultrahigh-vacuum cluster source system[20]. The charged particles were focused and mass selected in flight

15   prior to deposition onto a polycrystalline gold support for electrochemical measurements and onto

16   transmission electron microscope (TEM) grids for morphology investigations (Fig. 1a, Methods and

17   Supplementary Fig. 1)[20]. Annular dark-field scanning transmission electron microscope (ADF-STEM)

18   images show that the prepared Ir-Ta nanoparticles (NPs) with a selected mass of 6.0×10^3, 1.2×10^4 and

19   6.0×10^5 amu are homogeneous and well dispersed on the TEM grid (Fig. 1b Supplementary Fig. 2). The

20   particle size distributions of 6.0×10^3, 1.2×10^4, and 6.0×10^5 amu Ir-Ta NPs were first estimated according

21   to the ADF-STEM images (Fig. 1c and Supplementary Fig. 3). The measured sizes of 6.0×10^3, 1.2×10^4

1   and 6.0×10^5 amu particles are 1.1 ± 0.4, 1.4 ± 0.5 and 6.4 ± 0.8 nm, respectively. Compared to the

2   calculated diameter (Supplementary Table 1), assuming a perfectly spherical particle with metal bulk

3   density[20], the measured sizes are slightly larger, which could be due to the surface oxidation of Ir-Ta NPs

4   after exposure to air. Notably, the morphology of the 6.0×10^3 and 1.2×10^4 amu particles shows a plate-

5   like structure, suggesting that the discrepancy of smaller particles of 6.0×10^3 and 1.2×10^4 amu might also

6   result from the deviation of the particle shape from the ideal sphere.

7   To gauge the accuracy of mass-selected synthesis, the particle sizes of 6.0×10^3 and 1.2×10^4 amu Ir-

8   Ta NPs were further quantified via an atom-counting method utilizing the total amount of intensities

9   scattered by each atomic column. Details are described in Supplementary Fig. 4. As such, the total number

10 of Ir and Ta atoms in a particle could be obtained, as shown in Fig. 1d,e. Based on the investigations, the

11 number of atoms in a 6.0×10^3 or 1.2×10^4 amu Ir-Ta NP has been estimated to be 31 ± 2 or 67 ± 6 atoms,

12 respectively (Supplementary Figs. 5 and 6), which is consistent with the estimated numbers of 33 and 66

13 atoms based on their individual atomic masses, respectively. STEM energy-dispersive X-ray spectroscopy

14 (STEM-EDS) elemental mapping (Supplementary Figs. 7 and 8) confirms that Ir and Ta are

15 homogeneously distributed within each particle.

16   Prior to the electrochemical measurements, the as-deposited mass-selected Ir-Ta NPs on the gold

17 support were thermally annealed in air at 400 °C for 5 min (Supplementary Figs. 9 and 10). An elemental

18 composition of Ta/Ir = 9:1 and the overall distribution of the deposited NPs were characterized by X-ray

19 photoelectron spectroscopy (XPS; Supplementary Figs. 11-14). Figure 1f shows the XPS spectra of the

20 Ta $4f$ and Ir $4f$ core-level regions of the as-deposited Ir-Ta NPs and oxidized Ir-Ta-O NPs. The Ta $4f_{7/2}$

21 spectrum of the as-deposited sample shows a double set of peaks, suggesting a mixed oxidation state of

1   Ta, which is likely induced by trace amounts of water in the XPS chamber. The O $1s$ spectrum of the as-

2   deposited sample is shown in Supplementary Fig. 15. The high-resolution spectrum of the Ir $4f$ core-level

3   region of the as-prepared sample, after data processing due to Au $5p$ peak overlaps (Supplementary Figs.

4   11 and 12), suggests that Ir is in a metallic state. After oxidation, a clear positive shift in binding energy

5   can be observed for the Ta $4f_{7/2}$ and Ir $4f_{7/2}$ to 26.3 eV and 61.3 eV, which are consistent with Ta^{5+} and

6   Ir^{4+}, respectively. In this work, the oxidized Ir-Ta-O is denoted as $Ir_{0.1}Ta_{0.9}O_{2.45}$. To avoid the particle

7   overlap, the loading of the electrode is controlled to be 5% projected surface area coverage. The total mass

8   loadings of 60 to 275 ng cm^{-2} corresponding to an Ir loading of ~6 to 29 ng cm^{-2} (according to the elemental

9   ratio of Ta/Ir = 9:1) was precisely controlled by monitoring the particle beam current during the deposition

10   (Supplementary Table 1).

11   **Monitoring oxygen evolution on $Ir_{0.1}Ta_{0.9}O_{2.45}$ electrocatalysts.** The oxygen evolution performances of

12   the thermally oxidized $Ir_{0.1}Ta_{0.9}O_{2.45}$ catalysts were investigated in 0.1 M perchloric acid electrolyte

13   ($HClO_4$, pH = 1.08) by a Si-microchip-based EC-MS, which is schematically depicted in Fig. 2a. To avoid

14   the oxidation of the carbon support causing the overestimation of the OER activity (Supplementary Fig.

15   16), the polycrystalline gold with good conductivity and high corrosion resistance in acid was used as the

16   working electrode in this study. However, the formation of the tunnelling barrier of gold oxide with a wide

17   bandgap of 1.90 eV (Supplementary Fig. 17) at high anodic potential above 1.5 V versus a reversible

18   hydrogen electrode (RHE)[22] would compromise the electron transfer during OER working conditions,

19   resulting in a sluggish activity of the catalyst.

1   To investigate the OER activity of the catalysts without the influence of the tunnelling barrier of gold

2   oxide, the working potential range of the cyclic voltammetry (CV) tests was conducted between a cathodic

3   potential limit of 0.75 V versus RHE, near the initial the open-circuit potential (OCP) of the sample and

4   an anodic potential limit of 1.7 V versus. RHE. The low cathodic potential limit could inhibit the formation

5   of the tunnelling barrier and ensure a well-conductive electrode surface (Supplementary Figs. 18-20).

6   Figure 2b shows the CV of gold-supported 1.2×10^4 amu $Ir_{0.1}Ta_{0.9}O_{2.45}$ catalyst with the corresponding

7   electrochemical current (I_E) and the O_2 current (I_{O_2}, the current equivalent of the MS signal of the mass-

8   to-ratio $m/z=32$). It can be readily seen that I_E is relatively higher than I_{O_2} at anodic working potentials,

9   which is mostly due to the gold oxidation during OER (Supplementary Fig. 21). By integrating the MS O_2

10   currents ($m/z=32$) and Au reduction currents, we calculated the faradaic efficiency (FE) of the OER and

11   Au oxidation. The mass spectrometer signals of O_2 and CO_2, were calibrated internally for each

12   experiment, as shown in Supplementary Fig. 22. As shown in Fig. 2c, the FE values of the OER and Au

13   oxidation are 50 ± 4 % and 45 ± 4 %, respectively. The residual current goes towards adventitious carbon

14   decomposition and Au dissolution (Supplementary Fig. 23)[23].

15   Due to mass-transport effects, the measured MS currents do not directly correspond to the partial

16   current of the analyte under the dynamic conditions of CV measurements. This effect, however can be

17   eliminated by back calculating the partial current density from a measured MS current by a mathematical

18   deconvolution method (Supplementary Figs. 24 and 25), which has been demonstrated and validated in

19   our recent work[24]. After deconvolution (Fig. 2d), the obtained oxygen partial current presents the real

20   interfacial oxygen production rate under dynamic operating conditions. The lower activity of the cathodic

21   sweep of the deconvoluted O_2 current can most likely be ascribed to the formed tunnelling barrier of the

Au support at high working potentials. We therefore assessed the oxygen evolution activity of mass-selected catalysts by using the forward-moving, anodic sweep of the deconvoluted O_2 current (Supplementary Figs. 26 and 27).

Oxygen evolution performance of $Ir_{0.1}Ta_{0.9}O_{2.45}$ catalysts. The OER activity of mass-selected $Ir_{0.1}Ta_{0.9}O_{2.45}$ catalysts was evaluated using the mass activity (normalized to the total Ir loading) at 320 mV overpotential. Three different sizes of mass-selected IrO_2 catalysts within 1-2 nm were also studied for comparison (Supplementary Fig. 28), which shows an average mass activity of 650 ± 150 A_{O_2} g_{Ir}^{-1} at 320 mV overpotential. As shown in Fig. 3a, the mass activity of $Ir_{0.1}Ta_{0.9}O_{2.45}$ catalysts exhibit a marked enhancement of 1.2 ± 0.5 kA_{O_2} g_{Ir}^{-1} over pure IrO_2 within the same size range. Notably, the particle size of $Ir_{0.1}Ta_{0.9}O_{2.45}$ has a profound impact on the OER activity; a rapid decline of the OER activity is observed when the particle mass is higher than 4.4×10^4 amu (equivalent diameter, 2 nm). This lower activity is likely due to a compromised electrical conductivity in larger particles or surface segregation of Ta oxide. In addition, the pure Au electrode and mass-selected Ta_2O_5 catalysts were also studied, which are unsurprisingly inactive for the OER at low overpotentials (Supplementary Fig. 29).

A comprehensive comparison with other reported ruthenium- (Ru-) and Ir-based acidic OER catalysts is shown in Fig. 3b. Although the Ru-based catalysts are more active, the narrow potential region of the catalysts' stability (~0.7 to 1.4 V versus RHE, pH=1) severely hinders its practical applications[25]. The mass-selected $Ir_{0.1}Ta_{0.9}O_{2.45}$ with a highly reduced Ir loading exhibits a high mass activity in acid and comparable to state-of-the-art Ir-based catalysts. Several studies in the literature report higher activities. However, most of these studies have not actually measured the amount of evolved oxygen at the high

1   activity. Relying only on the measured CV will introduce large errors in the catalytic activity due to the

2   capacitance effect, redox couples, and corrosion. Therefore, a proper quantification of the OER activity is

3   to measure the oxygen evolution rate, as done in this work.

4   **Stability of mass-selected $Ir_{0.1}Ta_{0.9}O_{2.45}$ catalysts.** The operating stability of a catalyst is another

5   important metric for practical application. We investigated the stability of mass-selected $Ir_{0.1}Ta_{0.9}O_{2.45}$

6   catalyst by a long-term measurement at 1.6 V versus RHE for 24 h in 0.1 M $HClO_4$ (Fig. 4a). The working

7   electrode was initially held at OCP and stepped up for chronoamperometry at 1.6 V for 4 h; the OER

8   activity of mass-selected $Ir_{0.1}Ta_{0.9}O_{2.45}$ catalyst dropped quickly, within minutes (Supplementary Fig. 30),

9   in line with the deactivation observed for the gold-supported Ir-Au-TiO_2 catalyst[26]. We found the OER

10   activity of our catalyst could be recovered with negligible changes even after repeating five cycles by

11   reducing the Au electrode at OCP. Our recent work on the Pt electrode for OER shows that the tunnel

12   barrier for electron transfer by the formation of PtO_2 reduces the faradaic reaction rate of oxygen

13   evolution[24]. We therefore speculate that the gradual degradation of the OER activity during

14   chronoamperometry measurement is attributed to the formation of an insulating gold oxide layer rather

15   than the catalyst deactivation.

16   The stability number (*S*-number) of an electrocatalyst has been proposed as a metric to assess the

17   stability of catalysts, which compares the evolved oxygen (n_{O_2}, calculated according to the total charge

18   (Q_{total}) or MS O_2 currents) to the amount of dissolved Ir (n_{Ir}; ref. [27]). As shown in Fig. 4b, the *S*-numbers

19   of mass-selected $Ir_{0.1}Ta_{0.9}O_{2.45}$ NPs and sputtered $Ir_{0.1}Ta_{0.9}O_{2.45}$ thin film are calculated to be

20   approximately 10^6 (Supplementary Fig. 31), which is comparable with the reported rutile IrO_2 (~10^6, Alfa-

1   Aesar) and one order of magnitude higher than the rutile IrO_2 ($\sim 10^5$, Sigma-Aldrich) and other reported

2   Ir-based perovskites ($\sim 10^5$)[27-29]. In addition, STEM and XPS characterizations of mass-selected 1.2×10^4

3   amu $Ir_{0.1}Ta_{0.9}O_{2.45}$ particles were performed after the electrochemical measurements, which show no

4   significant changes in the morphology, distribution or composition of mass-selected $Ir_{0.1}Ta_{0.9}O_{2.45}$

5   catalysts (Supplementary Figs. 32 and 33), confirming the robust stability. Together, these results suggest

6   the $Ir_{0.1}Ta_{0.9}O_{2.45}$ catalysts have an excellent OER activity and stability in acid.

7   **Investigation of intrinsic activities.** To evaluate the potential for scalability and compare the intrinsic

8   activity of our catalysts to the literature, it is essential to assess the TOF, which quantifies how many

9   molecules O_2 are evolved per second per site at a specific overpotential[4]. Besides capacitive cycling and

10   porosimetry techniques, the CO stripping analysis is commonly used to determine the electrochemically

11   active surface area, especially for noble-metal catalysts[30]. In contrast with metallic noble-metal catalysts,

12   where the active site can be carefully explored, the assessment of oxides is rather complex due to the

13   pseudocapacitance charging processes during CO adsorption and oxidation[31]. Additionally, the loading

14   level of our system, below nanomolar, makes an accurate and precise characterization even more

15   challenging.

16   To overcome these difficulties, we employed the highly sensitive in-situ EC-MS technique to

17   determine the active sites rather than relying on the electrochemical current changes[21]. Furthermore, an

18   isotope-labelled ^{13}CO gas was introduced as a probe molecule, to exclude the interference of the

19   adventitious carbon from the system. According to the MS-monitored $^{13}CO_2$ signal, which comes from

20   only the oxidation of the adsorbed ^{13}CO on the active Ir sites, the number of surface active sites of the

21   $Ir_{0.1}Ta_{0.9}O_{2.45}$ catalyst can be quantified by integrating the corresponding MS current of $^{13}CO_2$ ($m/z = 45$)

signal for the intrinsic activity evaluation. The catalyst was brought to a potential of 0 V versus RHE to reduce the surface iridium atoms for CO adsorption[32]. In addition, pure mass-selected Ta_2O_5 NPs on a Au support do not show any ^{13}CO stripping signal, which indicates that all of the $^{13}CO_2$ signal must be associated with iridium. We assumed one ^{13}CO molecule adsorbed per surface iridium atom as supported by DFT (Supplementary Fig. 34). The experimental details are presented in Supplementary Figs. 35 and 36. For instance, the total Ir loading of 1.2×10^4 amu $Ir_{0.1}Ta_{0.9}O_{2.45}$ NPs with 5 % coverage on a Au support is ~8.0 pmol (4.8×10^{12} Ir atoms), and the number of surface Ir sites determined from the ^{13}CO stripping is 1.5×10^{12}, which means ~31 % Ir atoms are exposed on the surface. As shown in Fig. 5a, the mass-selected $Ir_{0.1}Ta_{0.9}O_{2.45}$ NPs in a small size regime (< 2 nm) have a similar surface Ir ratio of ~20-40 %, since essentially all atoms are residing at the surface. Contrarily when the particle size increases, more Ir atoms are trapped inside the particles during oxidation process[33], which results in a low surface Ir ratio of 3 % for 6.0×10^5 amu (equivalent diameter: 4.8 nm) particles.

Based on the MS-determined O_2 production rate, the TOF values were calculated according to the total Ir mass (TOF_{bulk}) and ^{13}CO-stripping-determined surface active sites ($TOF_{surface}$) of mass-selected $Ir_{0.1}Ta_{0.9}O_{2.45}$ NPs at 320 mV overpotential, displayed in Fig. 5b. We find that mass-selected $Ir_{0.1}Ta_{0.9}O_{2.45}$ NPs within a smaller size range (1-2 nm) yield similar intrinsic activities with a high average $TOF_{surface}$ value of 2.3 s^{-1}, which is four times higher than that of TOF_{bulk} (~0.6 s^{-1}); the $TOF_{surface}$ of 6.0×10^5 amu (~0.37 s^{-1}) is about 40 times higher than that of TOF_{bulk} (~0.01 s^{-1}), indicating the crucial impact of the particle size on the OER activity. As shown in Fig. 5c, the average $TOF_{surface}$ of mass-selected $Ir_{0.1}Ta_{0.9}O_{2.45}$ NPs within a smaller size range (1-2 nm) was compared to the state-of-the-art Ir/Ru-based OER catalysts in acidic media, the reported OER catalysts with superior activities need to be further

confirmed by measuring the evolved O_2 at certain potentials. Contrary to those Ir-based thin-film catalysts, the mass-selected $Ir_{0.1}Ta_{0.9}O_{2.45}$ NPs with considerably reduced Ir loading possess an intrinsic activity of 2.3 ± 0.9 s^{-1} at 320 mV overpotential, placing them among the most active Ir-based OER catalysts in acid.

DFT calculations. We further performed DFT calculations to gain insight into the OER activity and stability of the $Ir_{0.1}Ta_{0.9}O_{2.45}$ catalysts. The OER activity was evaluated using the theoretical overpotential calculation based on the acidic OER mechanism (Supplementary Fig. 37 and Supplementary Note 1)[34,35]. Due to the low Ir surface concentration of our catalysts, $Ir_{0.1}Ta_{0.9}O_{2.45}$ was first modelled using an Ir-doped Ta_2O_5 (200) surface with three distinct Ir-doping concentrations at the topmost surface (Fig. 6a). The Au-supported Ir-doped Ta_2O_5, pure IrO_2, pure Ta_2O_5 and Au-supported Ta_2O_5 were calculated for comparison (Fig. 6b,c and Supplementary Fig. 38). The calculated theoretical overpotentials of these structures as a function of the usual OER activity descriptor, the adsorption free energy difference between *O and *OH, are shown in Fig. 6d (ref. [34]). By comparing the calculated theoretical overpotentials of Ir-doped Ta_2O_5 (200) (0.45 V) and Ta_2O_5 (200) (0.93 V) to the Au-supported Ir-doped Ta_2O_5 (0.44 V) and Ta_2O_5 (200) (0.91 V), we find that the Au support has little effect on the OER catalytic activity. In addition, Ir-doped Ta_2O_5 (200) surfaces with different Ir-doping concentrations yield a theoretical overpotential similar to that (0.49 V) of IrO_2 (110) and the lowest Ir-doping surface (0.08 monolayer) possesses a favorable activity with a theoretical overpotential of 0.43 V.

We also investigated the OER activity for some cluster models and their calculated theoretical overpotentials are similar to those of Ir-doped Ta_2O_5 (200) and IrO_2(110). (Supplementary Fig. 39, Supplementary Note 2 and Supplementary Tables 3 and 4). These results suggest Ir-doped Ta_2O_5 would

have an OER activity as good as IrO_2. Note that we do not expect a direct quantitative comparison of the experimental and calculated theoretical overpotentials to match. The former is a potential-scale measure of the activity, while the latter is a function of the current density. Previous studies reported that higher octahedral distortion and undercoordinated Ir atoms are beneficial for catalytic activity[36,37]. We thus examined the local environment of the active Ir sites of modelled structures (Supplementary Fig. 40). We find that the structural motif of Ir in Ta_2O_5 (200) surface shows a distorted octahedron (IrO_6), which is similar to that in rutile IrO_2 (110). These results indicate that these special Ir local coordinations of $Ir_{0.1}Ta_{0.9}O_{2.45}$ catalysts may be responsible for the excellent OER activity, confirming the experimental observations.

In addition, the stability of the $Ir_{0.1}Ta_{0.9}O_{2.45}$ catalysts was evaluated by the calculated Pourbaix decomposition free energy (ΔG_{pbx}) using the DFT-calculated bulk Pourbaix diagram (Supplementary Fig. 41 and Supplementary Note 3)[38]. The calculated ΔG_{pbx} involves contributions from the phase stability and aqueous dissolution energy, the latter of which mainly determines the catalyst stability in the aqueous solution. Whether using the Ir-doped Ta_2O_5 bulk or surface/cluster phase of Ir-doped Ta_2O_5 will only affect the calculated phase stability, not the aqueous dissolution energy. Figure 6f shows the calculated aqueous decomposition free energies (ΔG_{pbx}) of Ir-doped Ta_2O_5 and IrO_2. Comparing with the calculated ΔG_{pbx} of IrO_2 (ref. [25]), the Ir-doped Ta_2O_5 has a non-zero ΔG_{pbx} (~0.2 eV per atom) at the potential 1.23 V to 1.60 V, which is attributed to its metastability (phase stability) compared to the stable phases of IrO_2 and Ta_2O_5. At the potential range of 1.60 to 1.82 V, the Ir-doped Ta_2O_5 decomposes to IrO_4^- + Ta_2O_5 (s) with a marginal increase of ΔG_{pbx}, suggesting that Ir-doped Ta_2O_5 could be stabilized by the slow phase transition to Ta_2O_5 (s) at room temperature. At potentials higher than 1.82 V, ΔG_{pbx} significantly increases,

and Ir-doped Ta_2O_5 decomposes to IrO_4^- + Ta_2O_7 (s). In this scenario, the Ir-doped Ta_2O_5 would suffer from a very large thermodynamic decomposition driving force and consequently becomes unstable in the aqueous solution. In the experiment, $Ir_{0.1}Ta_{0.9}O_{2.45}$ catalysts show much better stability than IrO_x catalysts, which can therefore be attributed to the smaller ΔG_{pbx}. Finally, although the exact structure of the $Ir_{0.1}Ta_{0.9}O_{2.45}$ NP is unknown, we believe these theoretical insights could shed light on the underpinning mechanisms of the enhanced OER performance.

Conclusions

In summary, we have synthesized a series of mass-selected $Ir_{0.1}Ta_{0.9}O_{2.45}$ acidic OER catalysts with an Ir loading of 9 wt% with an ultrahigh-vacuum cluster source. We have unambiguously evaluated the real OER activity of the gold-supported $Ir_{0.1}Ta_{0.9}O_{2.45}$ NPs using the microchip-based EC-MS instrument. We have found that mass-selected $Ir_{0.1}Ta_{0.9}O_{2.45}$ NPs with a size smaller than 2 nm exhibit an enhanced OER activity in 0.1 M $HClO_4$ with remarkable stability over 24 hours at 1.6 V versus RHE. The number of surface active Ir atoms was determined by the isotope-labelling combined EC-MS technique, and the mass-selected $Ir_{0.1}Ta_{0.9}O_{2.45}$ catalyst also demonstrates high intrinsic activity with a TOF value of 2.3 ± 0.9 s^{-1} at 320 mV overpotential. The good OER performance of our catalyst in acid can be explained by the favorable particle size and good Ir dispersion on the surface, as well as the favorable atomic configuration of the OER active center. We anticipate that our findings may apply to other wide-bandgap and corrosion-resistant metal oxides with well-controlled structures, thus accelerating the development of new low-cost, stable, and efficient acidic OER electrocatalysts.

Methods

Preparation of mass-selected Ir, Ta, and Ir-Ta particles. Pure Ir sputtering target (99.9%, Kurt J. Lesker), pure Ta target (99.95%, Kurt J. Lesker), and alloy Ir-Ta (Ir/Ta = 10:90 at%; 99.95%, ACI Alloys) were used to prepare the Ir, Ta, and Ir-Ta NPs, respectively. The NPs were prepared by a cluster source based on a direct current magnetron plasma sputtering and gas-aggregation (Teer Coating). The charged NPs of different sizes were extracted and focused by electrostatic lenses, and then passed through a lateral time-of-flight mass filter (with a mass resolution of $m/\Delta m = 20$). The distribution of available particle sizes can be tuned by changing the experimental parameters. The mass-selected NPs were deposited on TEM grids coated with ultra-thin carbon membrane (3 nm, Agar Scientific) or on 5-mm-diameter polycrystalline gold electrodes. For using Au supports, the polished surface was cleaned by 1.5 kV Ar^+ sputtering for 2 h to remove any residual contaminations, and XPS was used to check the cleanness before the deposition. The whole process including the precleaning, preparation and deposition, weas conducted in a multichamber under ultrahigh vacuum with a base pressure in the low 10^{-9} mbar region. Here, we assume each charged particle carries $1e$ charge, and thus the total loading of the deposited particles could be calculated according to the deposition current:

$$M_{Total} = mIt$$

Where M_{total} is the total loading of the deposited particles, m is the single NP mass, I is the deposition current and t is the deposition time. For the calculation of particle size, we assume a sphere structure of generated particle with bulk density[20]. In this study, the loading of the electrode is 5% projected surface area coverage.

Material characterizations. ADF-STEM images and STEM-EDS elemental maps were acquired using an aberration-corrected 'cubed' Thermo Fischer Scientific Titan electron microscope, operated at 200 kV, equipped with the ChemiSTEM system[39]. The probe convergence semi-angle and the detector collection inner semi-angle were set to 21.4 mrad and 38 mrad, respectively. From each investigated atomic cluster, series of 512×512 images were acquired, using a scan time of 0.5 s per frame. XPS measurements were performed using a non-monochromatized Al Kα source (XR-50; 1486.7 eV) and concentric hemispheric analyser (Phoibos 100), manufactured by SPECS. The as-prepared NPs were directly analysed under

ultrahigh-vacuum conditions after the deposition. The thermal annealed NPs, as well as the NPs after electrochemical testing, were measured on the same XPS set-up mentioned above. The employed pass energy was 100 eV for the overview and 20 eV for the high-resolution spectra. All spectra were charged reference against the Au 4*f* peak at 84 eV and a Shirley background was chosen for the elemental quantification. CasaXPS software was used for all the XPS analysis. Details of XPS data analysis can be found in the Supplementary Figs. 11 and 12. Inductively coupled plasma MS was performed on a Thermo Scientific iCAP Q ICP-MS (Thermo Fisher Scientific) in the Kinetic Energy Discrimination mode.

EC-MS measurements. Electrolyte solutions (0.1 M $HClO_4$) were prepared from perchloric acid (70 %, Sigma-Aldrich) by addition of ultrapure water (18.2 MΩ.cm at 25 $^\circ$C; Merck). The $Hg/HgSO_4$ reference electrode was calibrated by measuring the OCP of a cleaned platinum disc in H_2-purging 0.1 M $HClO_4$ electrolyte. To avoid the oscillations from potentiostat and easy-to-correct ohmic losses, we introduced a conventional ohmic resistor of 100 Ω with the working electrode. Unless otherwise stated, helium (6.0, Air Liquide) was used as an auxiliary gas during EC-MS experiments. The isotope-labeled ^{13}CO ($\geq$99 atom %; Sigma-Aldrich) stripping measurements were conducted in 0.1 M $HClO_4$ solution. The catalysts were firstly cycled in He-saturated electrolyte between 0 to 1 V versus RHE. After obtaining stable cyclic voltammogram, the carrier gas was exchanged from He to ^{13}CO while holding the potential at 0 V versus RHE for 2 min (ref. [32]). Then, ^{13}CO was removed by purging pure He gas into the electrolyte for 2 h, and continuous CVs were measured at a scan rate of 5 mV s^{-1}, with the first one being the CO stripping process. The raw data for the ^{13}CO stripping experiment is shown in Supplementary Fig. 35a. After the ^{13}CO stripping measurements, the OER activity was measured by cycling the working electrode between OCP and 1.7 V versus RHE with a scan rate of 20 mV s^{-1} until a stable CV was obtained.

DFT calculations. Density functional theory calculations were performed using Vienna Ab initio Simulation Package (VASP)[40]. The revised Perdew-Burke-Ernzerhof was used for adsorption energy calculations[41]. The plane-wave energy cut-off was set to 400 eV. The electronic energy and structure relaxation were converged within 10^{-5} eV and 0.05 eV Å^{-1}, respectively. The crystal structure of orthorhombic λ-Ta_2O_5 was used to study the surface catalytic activity of Ir-doped Ta_2O_5 (ref. [42]). Surface models with a slab thickness of at least 10 Å were generated with a maximum Miller index of two using

the Python Materials Genomics (pymatgen) package[43]. A vacuum separation of 12 Å was added to the direction perpendicular to the surface. Two four-layers (200) surface models with cell sizes of 2 × 1 and 3 × 2 were used for Ir-doped Ta_2O_5. The Brillouin zone was sampled using a gamma-center k-point grid of 3 × 3 × 1 and 2 × 1 × 1 for the 2 × 1 and 3 × 2 supercell surface models, respectively. A four-layers rutile $IrO_2(110)$ surface with a k-point grid of 3 × 3 × 1 was used. The bottom two layers of the slab models were fixed at the bulk position. For the $Ta_2O_5(200)/Au(111)$ interface, a slab model with a four-layer $Ta_2O_5(200)$ and three-layer Au(111) interface was constructed to investigate the gold support effect on the OER activity. The lattice mismatch between $Ta_2O_5(200)$ and Au(111) is about 0.14%. The Brillouin zone was integrated using a gamma center k-point grid of 1 × 2× 1. The topmost two layers were relaxed, and the rest were fixed at the bulk position. The OER activity was evaluated by calculating the theoretical overpotential of the reaction mechanism proposed in refs. [34,35] and detailed in Supplementary Note 1. The computational results of cluster models are provided in the Supplementary Note 2. The bulk Pourbaix diagram was calculated using the Strongly Constrained and Appropriately Normed (SCAN) functional, which has been recently shown to accurately predict the aqueous stability of solids[44,25]. In SCAN calculations, the plane-wave energy cut-off was 520 eV. The electronic energy and structure relaxation were converged to 10^{-5} eV and 0.02 eV $Å^{-1}$, respectively.

Data availability.

The authors declare that all data supporting the findings of this study are available within the paper and its Supplementary Information files and on DTU Data (https://doi.org/10.11583/DTU.16818703.v1).

Author Contributions

I.C., J.K., and J.K.N. conceived and supervised the project. Y.-R.Z. and Z.W co-wrote the manuscript. Y.-R.Z. performed electrochemical tests and collected and analyzed the data. J.V., K.Z., T.-W.L., F.P., and N.M. S. performed the mass-selected nanoparticles preparation and XPS measurements. Z.W., A.C., M.A., and J.K.N. performed DFT calculations. K.K., D.H., and S.B. S., assisted EC-MS data analysis. T.A., P.L., and S.B. preformed STEM experiments. J.F. and S.V.A. performed quantitative analysis of STEM data. C.M. performed the inductively coupled plasma MS measurements. All authors discussed the results and assisted during manuscript preparation.

Competing interests

The authors declare no competing interests.

2
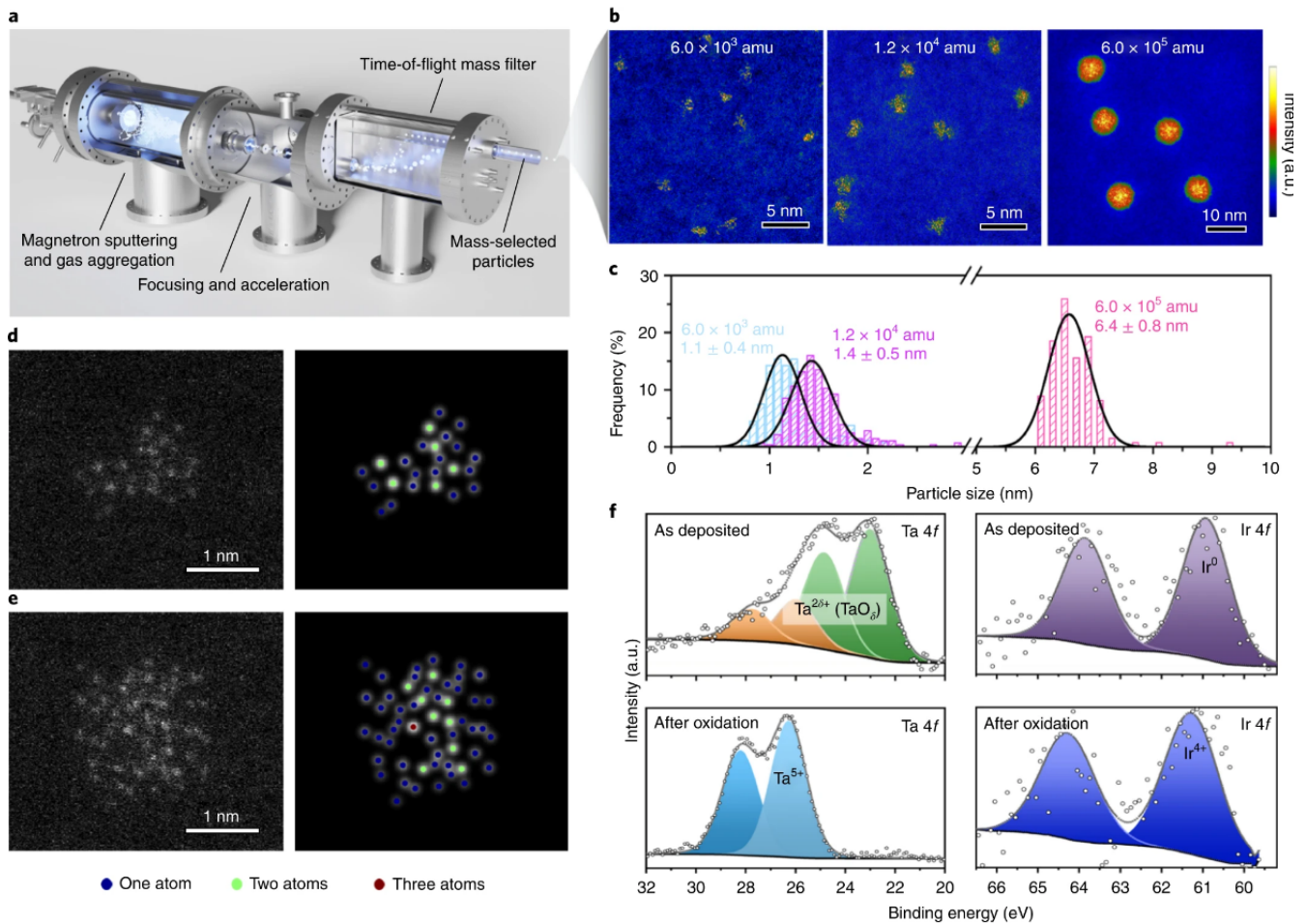
**Fig. 1 | Preparation and characterization of mass-selected Ir-Ta NPs. a,** Schematic illustration of the ultrahigh-
vacuum mass-selected cluster source technology, which comprises of a magnetron sputtering head, a noble gas-
aggregation chamber, a focusing and acceleration chamber and a time-of-flight mass filter. Mass-selected Ir-Ta NPs
were deposited on a polycrystalline gold electrode or TEM grids for further measurement. **b,** Representative ADF-
STEM images of three different masses of 6.0×10^3, 1.2×10^4 and 6.0×10^5 amu Ir-Ta NPs after exposure to air. **c,**
Size distributions of 6.0×10^3, 1.2×10^4 and 6.0×10^5 amu Ir-Ta NPs, which were determined by measuring the size in
the STEM images. **d,e,** Atomic scale high-magnification ADF-STEM images and corresponding optimized models
including atom counts for a 6.0×10^3 and 1.2×10^4 amu particle, respectively. The number of atoms was determined
by analyzing 12 and 26 different particles for the 6.0×10^3 and 1.2×10^4 amu Ir-Ta NPs respectively. **f,** XPS spectra
of Ta $4f$ and Ir $4f$ of 1.2×10^4 amu as-deposited sample and oxidized $Ir_{0.1}Ta_{0.9}O_{2.45}$ NPs. Background subtraction is
described in Supplementary Figs.11 and 12. The dots are the raw data and the grey line is the overall fitting envelope.
The same colours are used to indicate each couple of spin–orbit split components corresponding to a different
oxidation state.

16
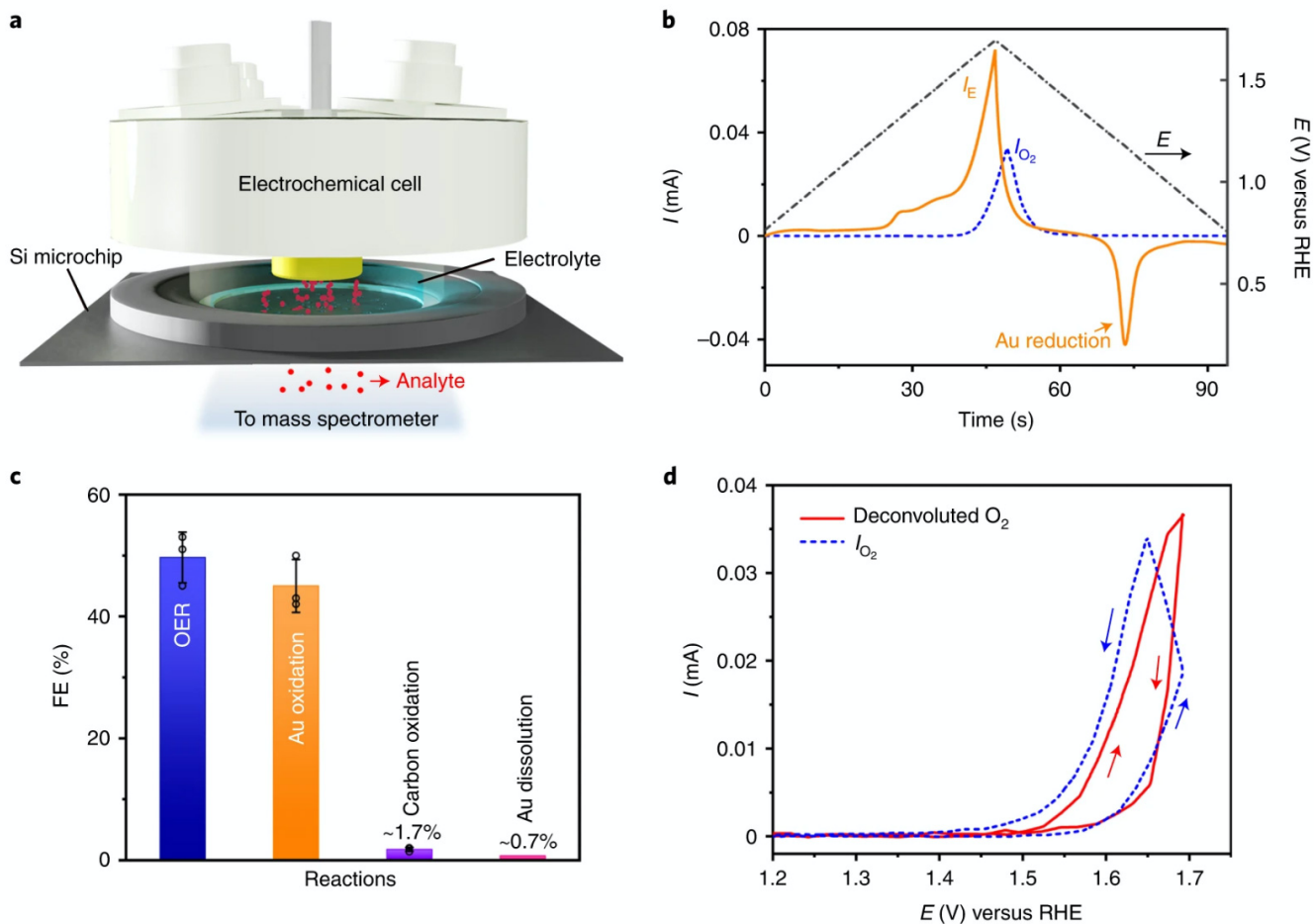
Fig. 2 | Monitoring oxygen evolution on gold supported mass-selected $Ir_{0.1}Ta_{0.9}O_{2.45}$ NPs. a, Schematic diagram of the electrochemical cell and Si-microchip assembly, which connects to the mass spectrometer. The distance between the working electrode and the microchip is ~100 μm. **b,** Comparison of the electrochemical current (I_E) and the O_2 current (I_{O_2}, back-calculated from MS signal of $m/z = 32$) of the 1.2×10^4 amu $Ir_{0.1}Ta_{0.9}O_{2.45}$ during potential (E) cycling between OCP and 1.7 V versus RHE with a scan rate of 20 mV s^{-1} in 0.1 M $HClO_4$. **c,** FE of each reaction of the $Ir_{0.1}Ta_{0.9}O_{2.45}$ catalyst during water oxidation within a working potential range of ~0.75-1.7 V versus RHE. The carbon decomposition is calculated from the MS monitored CO_2 products during potential cycling (Supplementary Fig. 23). The Au oxidation is calculated from the electrochemical Au reduction peak. The dissolved Au amount is ~10 ng cm^{-2} per cycle with an anodic limiting potential of 1.7 V versus RHE[23]. The error bars represent the Standard deviations of FE valuse of three independent samples (1.2×10^4, 1.26×10^4 and 4.4×10^4 amu). The scatter dots represent the individual values of the three experiments. **d,** Deconvoluted O_2 partial current in comparison to the measured O_2 current of the $Ir_{0.1}Ta_{0.9}O_{2.45}$ catalyst.
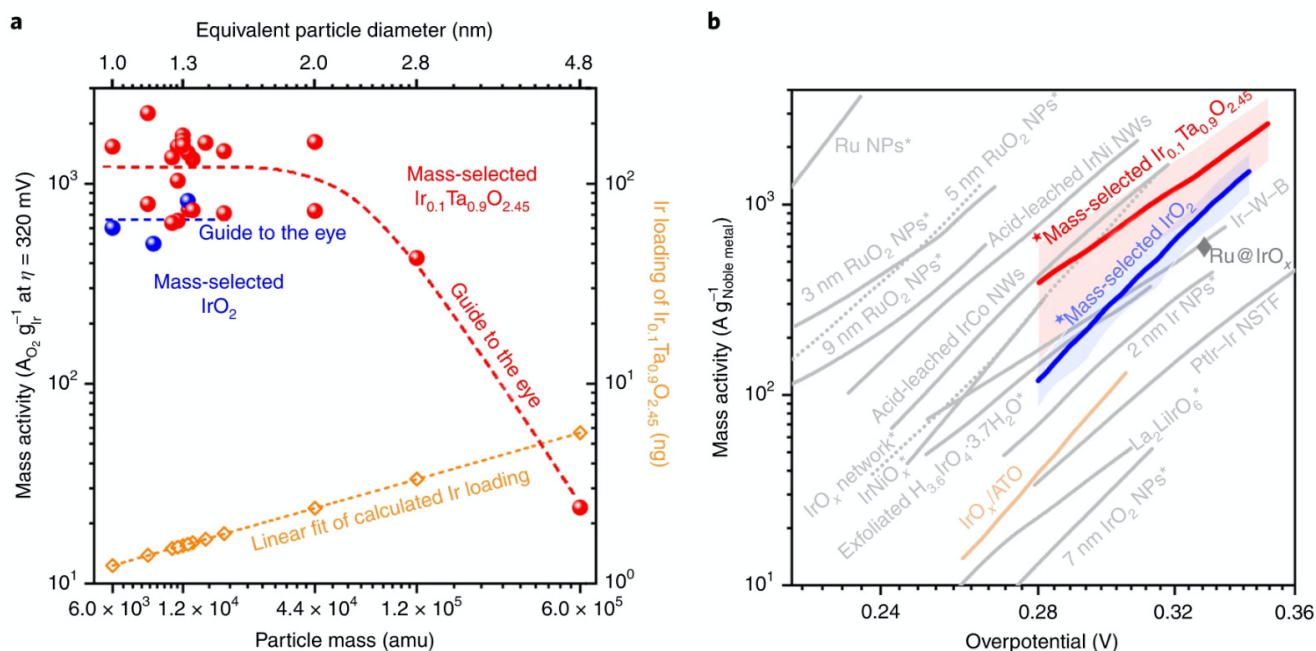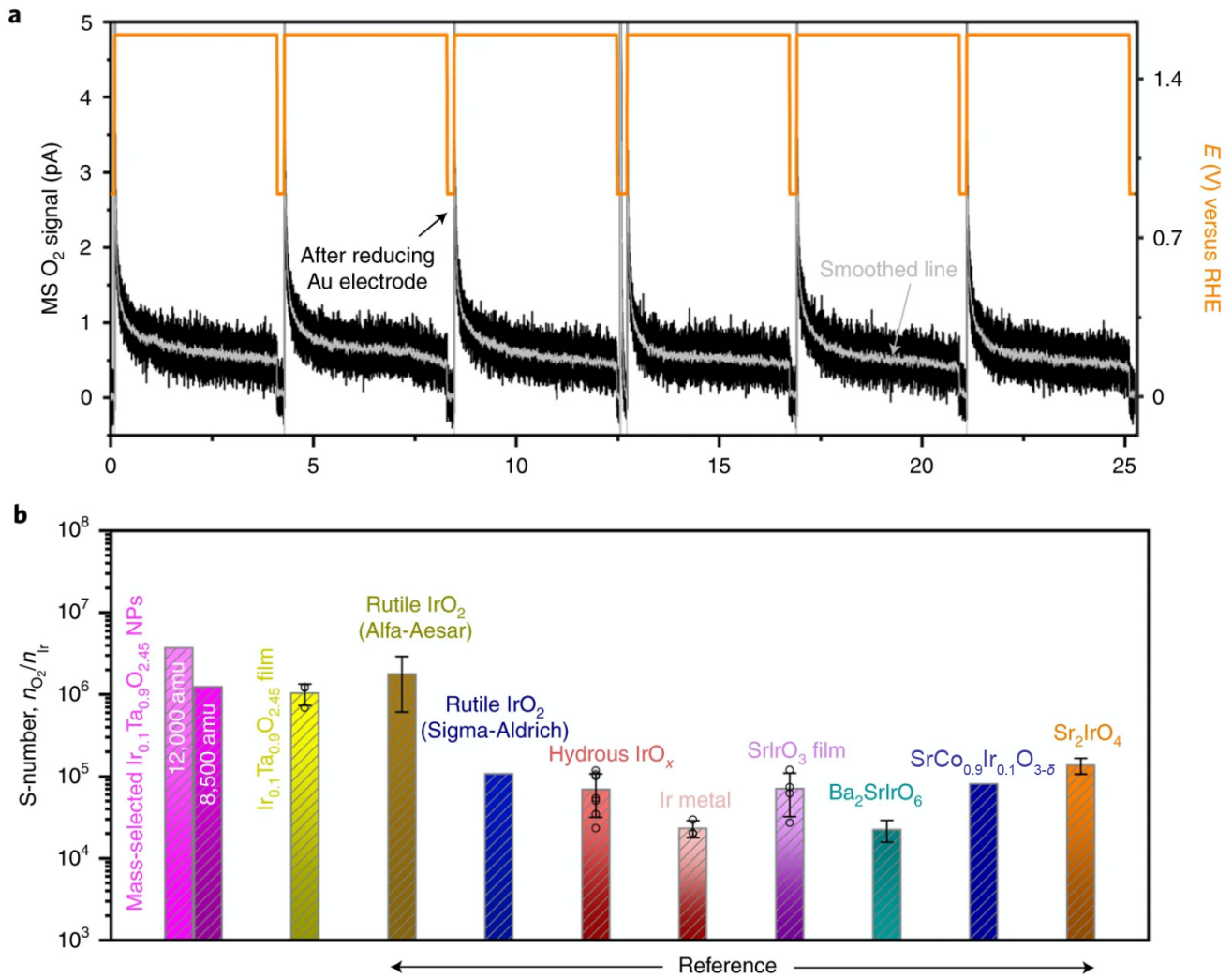
Fig. 3 | Comparison of OER catalytic performance. a, OER mass activities of mass-selected $Ir_{0.1}Ta_{0.9}O_{2.45}$ and IrO_2 NPs at 320 mV overpotential, and Ir loadings for different mass-selected $Ir_{0.1}Ta_{0.9}O_{2.45}$ NPs. The calculated Ir loading was determined from the deposition current; the linear fit line shown in orange has a slope of 0.33 and an R-squared (R^2, coefficient of determination) value of 0.999. The dotted lines shown in blue and red are guides to the eye. **b,** Comparison of mass activity between mass-selected $Ir_{0.1}Ta_{0.9}O_{2.45}$ and other state-of-the-art OER catalysts in acidic media. The average mass activity and standard deviation of mass-selected $Ir_{0.1}Ta_{0.9}O_{2.45}$ is based on 20 independent samples with sizes smaller than 4.4×10^4 amu (Supplementary Fig. 27). The average mass activity and standard deviation of mass-selected IrO_2 catalysts are based on three independent samples (6×10^4, 9×10^4 and 1.27×10^4 amu particles, Supplementary Fig. 28). The gray and orange lines are duplicated from the literatures: Ru NPs and 3, 5, and 9 nm RuO_2 NPs[45]; acid-leached IrNi and IrCo nanowires[46]; the IrO_x network[47]; Ir-W-B alloy[48]; 2 nm Ir NPs[49]; $IrNiO_x$ (ref. [13]); exfoliated $H_{3.6}IrO_4 \cdot 3.7H_2O$ (ref. [29]); IrO_x/antimony-doped tin oxide (ATO) (ref. [50]); PtIr-Ir nanostructured thin film (NSTF)[51]; 7 nm IrO_2 (ref. [52]); and La_2LiIrO_6 (ref. [53]). Diamond, $Ru@IrO_x$ (644.8 A g_{oxide}^{-1} @ 0.33 V overpotential)[54]. Asterisks, glassy-carbon-supported catalysts. Star, data from this work. The grey symbols represent the data that did not measure O_2, whereas the colored symbols represent the data that measured evolved O_2.

Fig. 4. | Stability of mass-selected Ir$_{0.1}$Ta$_{0.9}$O$_{2.45}$ NPs. a, Stability performance of the 4.4×10^4 amu Ir$_{0.1}$Ta$_{0.9}$O$_{2.45}$ catalyst at 1.6 V versus RHE for 24 h in 0.1 M HClO$_4$. After every 4 h, the working electrode was reduced at OCP for 10 min, and then stepped up to 1.6 versus RHE. The grey line is the smoothed curve derived from the MS O$_2$ currents (black line). **b,** Calculated S-number at 570 mV overpotential of mass-selected Ir$_{0.1}$Ta$_{0.9}$O$_{2.45}$ catalysts and other Ir-based thin film and powder OER catalysts in acid. Reference data are extracted from the literature: rutile IrO$_2$ (Sigma-Aldrich) and SrCo$_{0.9}$Ir$_{0.1}$O$_{3-\delta}$ (ref. [28]); rutile IrO$_2$ (Alfa-Aesar), hydrous IrO$_x$, Ir metal, SrIrO$_3$ film and Ba$_2$SrIrO$_6$ (ref. [27]); Sr$_2$IrO$_4$ (ref. [29]). The error bars of the Ir$_{0.1}$Ta$_{0.9}$O$_{2.45}$ thin film represent the standard deviation of the average S-number of three independent experiments. The scatter dots represent the individual values of the experiments. The evolved O$_2$ generated (n_{O_2}) during OER on mass-selected Ir$_{0.1}$Ta$_{0.9}$O$_{2.45}$ NPs is obtained from MS O$_2$ currents.
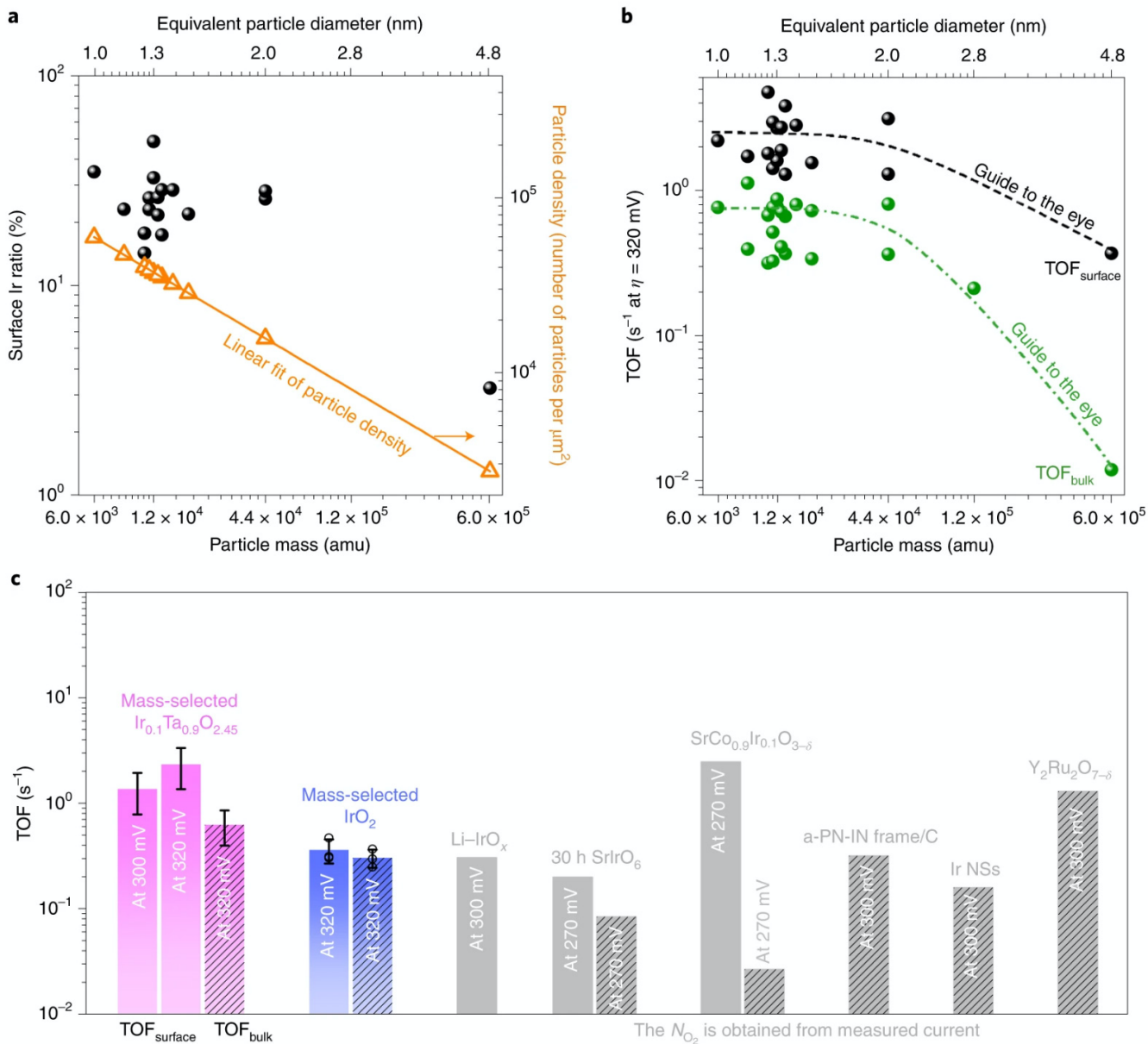
Fig. 5 | **Isotope-labelling coupled with EC-MS determined surface active sites and TOF values of mass-selected $Ir_{0.1}Ta_{0.9}O_{2.45}$ NPs. a,** In-situ ^{13}CO-stripping-determined surface Ir ratio and particle density as a function of the average particle mass of mass-selected $Ir_{0.1}Ta_{0.9}O_{2.45}$ NPs on a Au support. The particle density is calculated according to the deposition current; the linear fit line shown in orange has a slope of -0.67 and an R^2 value of 1. Under the same coverage (5%) on the Au support, the smaller the sample size, the higher the particle densities. **b,** TOF values calculated from total Ir mass (TOF_{bulk}, green) and the determined surface Ir atoms ($TOF_{surface}$, black) of mass-selected $Ir_{0.1}Ta_{0.9}O_{2.45}$ at 320 mV overpotential as a function of particle mass. Electrolyte, 0.1 M $HClO_4$. Scan rate, 20 mV s^{-1}. The dotted lines are guides to the eye. **c,** Comparison of TOF values between the mass-selected $Ir_{0.1}Ta_{0.9}O_{2.45}$ NPs, mass-selected IrO_2 NPs and reference noble-metal OER catalysts in acid, including Li-IrO_x (ref. [55]), 30 h $SrIrO_6$ (ref. [28]), $SrCo_{0.9}Ir_{0.1}O_{3-\delta}$ (ref. [28]), activated PtNi axis and IrNi edge frame catalyst (*a*-PN-IN frame/C)[56], amorphous Ir nanosheets (Ir NSs)[11] and $Y_2Ru_2O_{7-\delta}$ (ref. [57]). The colored columns represent the intrinsic

activity, which was determined by collecting the actually generated oxygen products, whereas the grey columns represent the number of O_2 molecules (N_{O2}) that is obtained from the measured electrochemical currents. Solid and hatch columns refer to experimentally/theoretically determined $TOF_{surface}$ and TOF_{bulk}, respectively. The error bars of the $TOF_{surface}$ values at 300 mV and 320mV overpotential of mass-selected $Ir_{0.1}Ta_{0.9}O_{2.45}$ represent the standard deviation of 16 independent samples with sizes smaller than 4.4×10^4 amu. The error bar of TOF_{bulk} at 320 mV overpotential of mass-selected $Ir_{0.1}Ta_{0.9}O_{2.45}$ represent the standard deviation of the average value of 18 independent samples with sizes smaller than 4.4×10^4 amu. The error bars of mass-selected IrO_2 represent the standard deviation of the average TOF of three independent samples (6×10^4, 9×10^4 and 1.27×10^4 amu). The scatter dots represent the individual values of the three experiments.
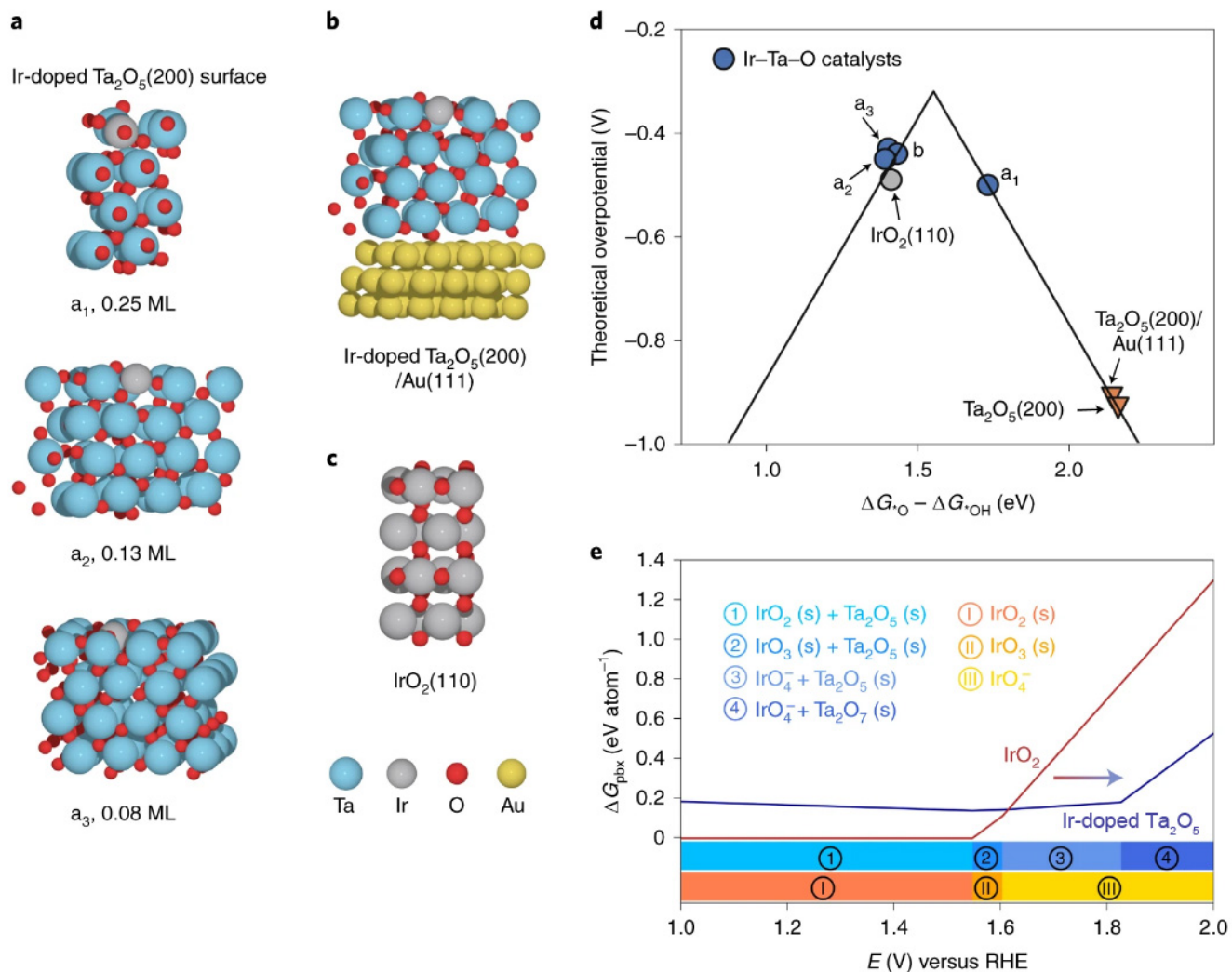
Fig. 6 | Theoretical analysis of OER activity and stability. a-c, Structure models used for catalytic activity calculations of Ir-doped Ta_2O_5(200) (**a**), Ir-doped Ta_2O_5(200)/Au(111) (**b**) and IrO_2(110) (**c**). The Ir-doping concentration at the topmost surface was represented by the fraction of a monolayer (ML). **d,** Theoretical overpotential volcano plot as a function of the OER activity descriptor characterized by the adsorption free energy difference between *O and *OH. The labelled data points correspond to the modelled structures in **a-c**. **e,** Calculated aqueous decomposition free energy (ΔG_{pbx}) of Ir-doped Ta_2O_5 and IrO_2 from the potential 1.0 to 2.0 V versus RHE at pH = 0. The projection of ΔG_{pbx} onto the potential axis presents the stable chemical species at the corresponding regions. The arrow is drawn to show the decreasing trend of ΔG_{pbx} with respect to the applied potential.

References

1   Seh, Z. W. *et al.* Combining theory and experiment in electrocatalysis: Insights into materials design. *Science* **355**, eaad4998 (2017).

2   Chu, S., Cui, Y. & Liu, N. The path towards sustainable energy. *Nat. Mater.* **16**, 16-22 (2017).

3   Ayers, K. E. *et al.* Research advances towards low cost, high efficiency PEM electrolysis. *ECS Trans.* **33**, 3-15 (2010).

4   Kibsgaard, J. & Chorkendorff, I. Considerations for the scaling-up of water splitting catalysts. *Nat. Energy* **4**, 430-433 (2019).

5   Carmo, M., Fritz, D. L., Mergel, J. & Stolten, D. A comprehensive review on PEM water electrolysis. *Int. J. Hydrogen Energy* **38**, 4901-4934 (2013).

6   Escudero-Escribano, M. *et al.* Importance of Surface IrO_x in Stabilizing RuO_2 for Oxygen Evolution. *J. Phys. Chem. B* **122**, 947-955 (2018).

7   Vesborg, P. C. & Jaramillo, T. F. Addressing the terawatt challenge: scalability in the supply of chemical elements for renewable energy. *RSC Adv.* **2**, 7933-7947 (2012).

8   Bernt, M. *et al.* Current Challenges in Catalyst Development for PEM Water Electrolyzers. *Chem. Ing. Tech.* **92**, 31-39 (2020).

9   Oakton, E. *et al.* IrO_2-TiO_2: A high-surface-area, active, and stable electrocatalyst for the oxygen evolution reaction. *ACS Catal.* **7**, 2346-2352 (2017).

10   da Silva, G. C. *et al.* Oxygen evolution reaction on tin oxides supported iridium catalysts: Do we need dopants? *ChemElectroChem* **7**, 2330-2339 (2020).

11   Wu, G. *et al.* A general synthesis approach for amorphous noble metal nanosheets. *Nat. Commun.* **10**, 4855 (2019).

12   Seitz, L. C. *et al.* A highly active and stable IrO_x/$SrIrO_3$ catalyst for the oxygen evolution reaction. *Science* **353**, 1011-1014 (2016).

13   Nong, H. N. *et al.* A unique oxygen ligand environment facilitates water oxidation in hole-doped IrNiOx core-shell electrocatalysts. *Nat. Catal.* **1**, 841-851 (2018).

14   Spoeri, C., Kwan, J. T. H., Bonakdarpour, A., Wilkinson, D. P. & Strasser, P. The stability challenges of oxygen evolving catalysts: towards a common fundamental understanding and mitigation of catalyst degradation. *Angew. Chem. Int. Ed.* **56**, 5994-6021 (2017).

15   Oakton, E. *et al.* A simple one-pot Adams method route to conductive high surface area IrO_2–TiO_2 materials. *New J. Chem.* **40**, 1834-1838 (2016).

16   Card, H. Potential barriers to electron tunnelling in ultra-thin films of SiO_2. *Solid State Commun.* **14**, 1011-1014 (1974).

17   Valden, M., Lai, X. & Goodman, D. W. Onset of catalytic activity of gold clusters on titania with the appearance of nonmetallic properties. *Science* **281**, 1647-1650 (1998).

18   Kim, Y.-T. *et al.* Balancing activity, stability and conductivity of nanoporous core-shell iridium/iridium oxide oxygen evolution catalysts. *Nat. Commun.* **8**, 1449 (2017).

19   Suntivich, J., May, K. J., Gasteiger, H. A., Goodenough, J. B. & Shao-Horn, Y. A perovskite oxide optimized for oxygen evolution catalysis from molecular orbital principles. *Science* **334**, 1383-1385 (2011).

20   Roy, C. *et al.* Impact of nanoparticle size and lattice oxygen on water oxidation on $NiFeO_xH_y$. *Nat. Catal.* **1**, 820-829 (2018).

21 Trimarco, D. B. *et al.* Enabling real-time detection of electrochemical desorption phenomena with sub-monolayer sensitivity. *Electrochim. Acta* **268**, 520-530 (2018).

22 Diaz-Morales, O., Calle-Vallejo, F., de Munck, C. & Koper, M. T. Electrochemical water splitting by gold: evidence for an oxide decomposition mechanism. *Chem. Sci.* **4**, 2334-2343 (2013).

23 Cherevko, S., Zeradjanin, A. R., Keeley, G. P. & Mayrhofer, K. J. A comparative study on gold and platinum dissolution in acidic and alkaline media. *J. Electrochem. Soc.* **161**, H822-H830 (2014).

24 Krempl, K. *et al.* Dynamic Interfacial Reaction Rates from Electrochemistry–Mass Spectrometry. *Anal. Chem.* **93**, 7022-7028 (2021).

25 Wang, Z., Guo, X., Montoya, J. & Nørskov, J. K. Predicting aqueous stability of solid with computed Pourbaix diagram using SCAN functional. *Npj Comput. Mater.* **6**, 160 (2020).

26 Regmi, Y. N. *et al.* Supported Oxygen Evolution Catalysts by Design: Toward Lower Precious Metal Loading and Improved Conductivity in Proton Exchange Membrane Water Electrolyzers. *ACS Catal.* **10**, 13125-13135 (2020).

27 Geiger, S. *et al.* The stability number as a metric for electrocatalyst stability benchmarking. *Nat. Catal.* **1**, 508-515 (2018).

28 Chen, Y. *et al.* Exceptionally active iridium evolved from a pseudo-cubic perovskite for oxygen evolution in acid. *Nat. Commun.* **10**, 572 (2019).

29 Zhang, R. *et al.* First Example of Protonation of Ruddlesden–Popper Sr_2IrO_4: A Route to Enhanced Water Oxidation Catalysts. *Chem. Mater.* **32**, 3499-3509 (2020).

30 Trasatti, S. & Petrii, O. Real surface area measurements in electrochemistry. *J. Electroanal. Chem.* **327**, 353-376 (1992).

31 Binninger, T., Fabbri, E., Kötz, R. & Schmidt, T. J. Determination of the electrochemically active surface area of metal-oxide supported platinum catalyst. *J. Electrochem. Soc.* **161**, H121-H128 (2013).

32 Scott, S. B., Kibsgaard, J., Vesborg, P. C. & Chorkendorff, I. Tracking oxygen atoms in electrochemical CO oxidation-Part II: Lattice oxygen reactivity in oxides of Pt and Ir. *Electrochim. Acta* **374**, 137844 (2021).

33 Herrada, R. A. *et al.* Characterization of Ti electrodes electrophoretically coated with IrO_2-Ta_2O_5 films with different Ir:Ta molar ratios. *J. Alloys Compd.* **862**, 158015 (2021).

34 Man, I. C. *et al.* Universality in oxygen evolution electrocatalysis on oxide surfaces. *ChemCatChem* **3**, 1159-1165 (2011).

35 Rossmeisl, J., Qu, Z.-W., Zhu, H., Kroes, G.-J. & Nørskov, J. K. Electrolysis of water on oxide surfaces. *J. Electroanal. Chem.* **607**, 83-89 (2007).

36 Willinger, E., Massué, C., Schlögl, R. & Willinger, M. G. Identifying Key Structural Features of IrO_x Water Splitting Catalysts. *J. Am. Chem. Soc.* **139**, 12093-12101 (2017).

37 Wan, G. *et al.* Amorphization mechanism of $SrIrO_3$ electrocatalyst: How oxygen redox initiates ionic diffusion and structural reorganization. *Sci. Adv.* **7**, eabc7323 (2021).

38 Singh, A. K. *et al.* Electrochemical stability of metastable materials. *Chem. Mater.* **29**, 10159-10167 (2017).

39 Schlossmacher, P., Klenov, D., Freitag, B. & Von Harrach, H. Enhanced detection sensitivity with a new windowless XEDS system for AEM based on silicon drift detector technology. *Micros. today* **18**, 14-20 (2010).

40 Kresse, G. & Furthmüller, J. Efficient iterative schemes for ab initio total-energy calculations using a plane-wave basis set. *Phys. Rev. B* **54**, 11169 (1996).

41 Hammer, B., Hansen, L. B. & Nørskov, J. K. Improved adsorption energetics within density-functional theory using revised Perdew-Burke-Ernzerhof functionals. *Phys. Rev. B* **59**, 7413-7421 (1999).

42 Lee, S.-H., Kim, J., Kim, S.-J., Kim, S. & Park, G.-S. Hidden structural order in orthorhombic Ta_2O_5. *Phys. Rev. Lett.* **110**, 235502 (2013).

43 Ong, S. P. *et al.* Python Materials Genomics (pymatgen): A robust, open-source python library for materials analysis. *Comput. Mater. Sci.* **68**, 314-319 (2013).

44 Sun, J., Ruzsinszky, A. & Perdew, J. P. Strongly constrained and appropriately normed semilocal density functional. *Phys. Rev. Lett.* **115**, 036402 (2015).

45 Paoli, E. A. *et al.* Oxygen evolution on well-characterized mass-selected Ru and RuO_2 nanoparticles. *Chem. Sci.* **6**, 190-196 (2015).

46 Alia, S. M., Shulda, S., Ngo, C., Pylypenko, S. & Pivovar, B. S. Iridium-Based Nanowires as Highly Active, Oxygen Evolution Reaction Electrocatalysts. *ACS Catal.* **8**, 2111-2120 (2018).

47 Jensen, A. W. *et al.* Self-supported nanostructured iridium-based networks as highly active electrocatalysts for oxygen evolution in acidic media. *J. Mater. Chem. A* **8**, 1066-1071 (2020).

48 Li, R. *et al.* IrW nanochannel support enabling ultrastable electrocatalytic oxygen evolution at $2\,A\,cm^{-2}$ in acidic media. *Nat. Commun.* **12**, 3540 (2021).

49 Nong, H. N., Gan, L., Willinger, E., Teschner, D. & Strasser, P. IrO_x core-shell nanocatalysts for cost-and energy-efficient electrochemical water splitting. *Chem. Sci.* **5**, 2955-2963 (2014).

50 Oh, H.-S. *et al.* Electrochemical Catalyst–Support Effects and Their Stabilizing Role for IrO_x Nanoparticle Catalysts during the Oxygen Evolution Reaction. *J. Am. Chem. Soc.* **138**, 12552-12563 (2016).

51 Debe, M. *et al.* Initial performance and durability of ultra-low loaded NSTF electrodes for PEM electrolyzers. *J. Electrochem. Soc.* **159**, K165-K176 (2012).

52 Lee, Y., Suntivich, J., May, K. J., Perry, E. E. & Shao-Horn, Y. Synthesis and activities of rutile IrO_2 and RuO_2 nanoparticles for oxygen evolution in acid and alkaline solutions. *J. Phys. Chem. Lett.* **3**, 399-404 (2012).

53 Grimaud, A. *et al.* Activation of surface oxygen sites on an iridium-based model catalyst for the oxygen evolution reaction. *Nat. Energy* **2**, 16189 (2016).

54 Shan, J. *et al.* Charge-Redistribution-Enhanced Nanocrystalline $Ru@IrO_x$ Electrocatalysts for Oxygen Evolution in Acidic Media. *Chem* **5**, 445-459 (2019).

55 Gao, J. *et al.* Breaking long-range order in iridium oxide by alkali ion for efficient water oxidation. *J. Am. Chem. Soc.* **141**, 3014-3023 (2019).

56 Choi, S. *et al.* Pt Dopant: Controlling the Ir Oxidation States toward Efficient and Durable Oxygen Evolution Reaction in Acidic Media. *Adv. Funct. Mater.* **30**, 2003935 (2020).

57 Kim, J. *et al.* High-performance pyrochlore-type yttrium ruthenate electrocatalyst for oxygen evolution reaction in acidic media. *J. Am. Chem. Soc.* **139**, 12076-12083 (2017).

Additional information

Supplementary information is available for this paper at http://XXXXXXXXX.

Reprints and permission information are available at XXX.